



A pilot-process for calcium hydroxide production from iron slag by low-temperature precipitation

Sara Vallejo Castaño^{a,b}, Erika Callagon La Plante^{b,c,d}, Marie Collin^{b,c}, Gaurav Sant^{b,c,e,f,*}, Laurent Pilon^{a,b,c,g,**}

^a Mechanical and Aerospace Engineering Department, University of California, Los Angeles, Los Angeles, CA 90095-1597, USA

^b Laboratory for the Chemistry of Construction Materials (LC²) Department of Civil and Environmental Engineering, University of California, Los Angeles, Los Angeles, CA 90095, USA

^c Institute for Carbon Management, University of California, Los Angeles, Los Angeles, CA 90095, USA

^d Department of Materials Science and Engineering, University of Texas at Arlington, Arlington, TX 76019, USA

^e Department of Materials Science and Engineering, University of California, Los Angeles, Los Angeles, CA 90095, USA

^f California Nano Systems Institute, University of California, Los Angeles, Los Angeles, CA 90095, USA

^g Institute of the Environment and Sustainability, University of California, Los Angeles, Los Angeles, CA 90095, USA

ARTICLE INFO

Keywords:

Calcium hydroxide
Portlandite
Reverse osmosis
Precipitation
Carbon capture

ABSTRACT

The production of Ca(OH)₂ via thermal decomposition of limestone is an energy intensive process resulting in significant CO₂ emissions. However, if produced in a manner that obviates the need for the thermal decomposition of limestone, Ca(OH)₂ could be a “CO₂-negative” material. Herein, we design and demonstrate the operation of a continuous, low-temperature (< 100 °C), aqueous-phase pilot-process to produce Ca(OH)₂ using calcium extracted from alkaline industrial wastes. The three-step process encompasses unit operations including: (i) calcium leaching from basic oxygen furnace BOF slag, (ii) leachate concentration by reverse osmosis (RO), and (iii) Ca(OH)₂ precipitation by temperature swing. This process presents several advantages compared to the traditional route. First, it advances the recycling of waste from the steel industry. Second, it operates significantly below the temperature used in conventional lime production (900 °C) as it bypasses limestone calcination, responsible for ~65% of the CO₂ emissions from the current process. Thus, the new process has a lower CO₂ footprint and enables the use of industrial waste heat. The mass and energy balances were quantified to reveal that increasing the calcium concentration of the feed solution and the precipitation temperature, decrease the energy demands of the RO step, thereby reducing the process's overall CO₂ footprint. The pilot system operated continuously and achieved a production rate of nearly 1 kg per day of Ca(OH)₂ with a purity greater than 95 wt %. The average particle size of the precipitates depended on the residence time in the precipitation reactor, demonstrating an ability to produce size-controlled particulates. Importantly, the process achieved full water recirculation/reutilization level indicative of a low-consumable water demand. The outcomes offer new insights and understanding relevant to developing and upscaling low-CO₂ processes for cement, lime, and portlandite.

1. Introduction

The use of lime CaO and hydrated lime Ca(OH)₂ as a construction material dates back to 6,000 years when it was used by the Egyptians for plastering the pyramids [1]. Besides cementation [2,3], lime finds an extensive number of applications including paper production [4], water treatment [5,6], iron ores processing [7], and soil pH regulation [8,9].

Additionally, hydrated lime (portlandite) can capture 59% of its weight in CO₂ when it undergoes carbonation [10,11]. Hence, Ca(OH)₂ could be a “CO₂-negative” material if its production process could emit less than 0.59 tons of CO₂ per ton of Ca(OH)₂. Making CO₂-negative Ca(OH)₂ could help decarbonize some industries. For example, partially replacing cement with supplementary cementitious materials and Ca(OH)₂ [12] could diminish the demand for ordinary Portland cement (OPC) whose production accounts for 7% of global anthropogenic CO₂ emissions [13].

* Corresponding author at: Laboratory for the Chemistry of Construction Materials (LC²) Department of Civil and Environmental Engineering, University of California, Los Angeles, Los Angeles, CA 90095, USA.

** Corresponding author at: Mechanical and Aerospace Engineering Department, University of California, Los Angeles, Los Angeles, CA 90095-1597, USA.

E-mail addresses: gsant@ucla.edu (G. Sant), pilon@seas.ucla.edu (L. Pilon).

<https://doi.org/10.1016/j.jece.2022.107792>

Received 3 February 2022; Received in revised form 22 April 2022; Accepted 22 April 2022

Available online 26 April 2022

2213-3437/© 2022 Elsevier Ltd. All rights reserved.

Nomenclature		X_{Ca}	Ca yield
A_m	membrane area (m ²)	<i>Greek Symbols</i>	
[Ca]	calcium concentration (mol/m ³)	φ_i	differential volume fraction
c_p	heat capacity of water (J/(kg·K))	η_p	pump hydraulic efficiency
d	slag particle size (μm)	η_{PC}	precipitation efficiency
D_I	impeller diameter (m)	$\Delta\pi$	osmotic pressure difference (Pa)
GSA	geometric surface area (cm ² /g)	ρ	density of water (kg/m ³)
L_p	membrane permeability (m ³ /(s·m ² ·Pa))	τ	duration of the continuous process (s)
\dot{m}	mass flow rate (kg/s)	ω	rotational frequency (s ⁻¹)
M	mass (kg)	<i>Subscript</i>	
M	molar mass (g/mol)	Cool	refers to cooling
N_b	number of leaching batches	C _{in}	refers to inlet cooling stream
N_p	mixing power number	C _{out}	refers to outlet cooling stream
P	pressure (Pa)	Ca(OH) ₂	calcium hydroxide
ΔP_{mem}	transmembrane pressure difference (Pa)	e	experimental
q	specific thermal energy (kWh/kg Ca(OH) ₂)	f	refers to final slag particle size
\dot{Q}	thermal power (kW)	F	feed stream
[OH ⁻]	hydroxyl ion concentration (mol/m ³)	g	grinding
R	rejection coefficient	heat	heating
R_U	universal gas constant (J/(mol·K))	i	refers to initial particle size
SA_i	particle surface area (cm ²)	L	leachate stream
T	temperature (K or °C)	m	mixing
V_i	particle volume (cm ³)	M	refers to mix stream
V_{precip}	precipitation reactor volume (m ³)	P	refers to precipitation or permeate stream
\dot{V}	volumetric flow rate (L/h or m ³ /s)	R	refers to retentate stream
W	specific energy consumption (kWh/kg)	S	refers to saturate stream
W	energy consumption (kWh)	slag	refers to slag
\dot{W}	power consumption (kW)		
W_b	bond work index		

According to the U.S. Geological Survey (USGS), 430 million tons of quick- and hydrated-lime were produced globally in 2019 [14]. However, its current production is energy intensive and a major emitter of CO₂ [9,15]. It also requires the use of limestone, a non-renewable mineral that fosters biodiversity in natural ecosystems [16]. To decrease the extent of extractive activities, the amount of energy needs and CO₂ emissions of lime production, we have previously developed a facile three-step route to produce Ca(OH)₂ from slag, an alkaline byproduct of the iron industry [17,18]. The process operated at low temperature (≤ 100 °C) and bypassed calcination, the most CO₂ emitting step of CaO and Ca(OH)₂ production.

In this calcination-free method, slag and water came in contact to obtain a solution with calcium concentration ([Ca]) ranging from 1 to 17 mmol/L (mM) [17]. Our previous study showed that achieving large calcium concentrations in solution by increasing the solid to liquid ratio during leaching came at the expense of calcium conversion [17]. Additionally, results indicated that the maximum calcium concentration that can be sustained in solution during leaching was lower than the saturation concentration of Ca(OH)₂ at room temperature, since the silicon leached also from slag captured the dissolved calcium through the precipitation of calcium silicate hydrate phases that have a lower solubility than Ca(OH)₂ [19–21]. Although the method developed was demonstrated with basic oxygen furnace (BOF) slag, other types of slag, fly ashes, and alkaline rock species can also release calcium through leaching [22–26]. The leachate was then concentrated through reverse osmosis (RO), wherein a membrane semipermeable to water rejects cations (e.g., Ca²⁺, Mg²⁺) by size and/or charge exclusion mechanisms [27], producing a permeate stream with low ionic concentration and enriching the retentate stream up to the saturation point of Ca(OH)₂ (~21.2 mmol/L at pH = 12.5 and T = 25 °C [28]). Batch RO experiments – wherein the concentration of the feed increases as a function of

time – indicated that after 6 h, membrane scaling hindered the concentration process, questioning the stability of the concentration step at longer times and larger scale. Finally, we demonstrated the precipitation of Ca(OH)₂ from the concentrated slag leachates by harnessing the decreasing solubility of Ca(OH)₂ with increasing solution temperature [29]. In total, we retrieved ~ 3 mg of precipitates from 0.5 L of solution with a purity of 66%. Although the quantity and purity of the synthesized Ca(OH)₂ crystals were low, achieving precipitation at sub-boiling temperature (< 100 °C) demonstrated that the process can be scaled up using underutilized low-grade waste heat from industrial facilities.

The proof-of concept of our process was demonstrated successfully on the laboratory scale, with each step demonstrated separately [17,18]. However, we did not show a continuous integrated process, a key step towards process intensification. In addition, the proposed process could have a large water footprint, requiring 5400 L of water per kg of Ca(OH)₂ produced. Thus, implementing water recirculation is essential to demonstrate that this technology is technically viable. The present study aims to scale-up the three-step Ca(OH)₂ production method previously developed [17] by demonstrating a continuous pilot system capable of producing up to 1 kg of Ca(OH)₂ per day. A steady-state model based on mass and energy conservation principles was used to select the operating conditions tested in the pilot system, and to assess the influence of calcium concentration and precipitation temperature on the process energy consumption and production throughput.

2. Materials and methods

2.1. Materials

2.1.1. Slag preparation and characterization

A mass of 500 kg of BOF slag was obtained from Stein Inc. (Ohio, U.

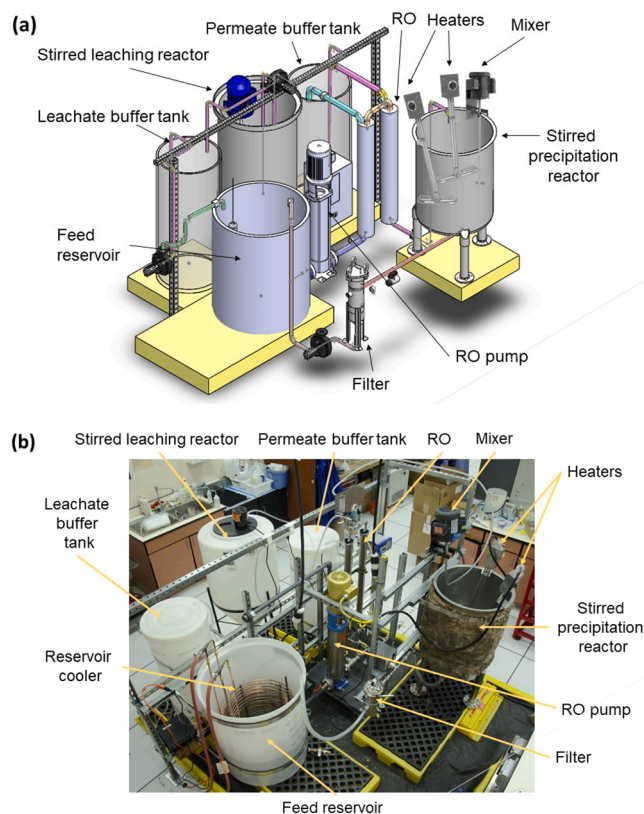


Fig. 1. (a) A rendering of the pilot system at UCLA and (b) a photograph of the experimental pilot system built to produce $\text{Ca}(\text{OH})_2$ from BOF slag.

S) and milled in 5 batches for 2 h by U.S. Stoneware (Ohio, U.S.) using a 27-gallon ball mill. The slag was then separated into different size fractions using a ro-tap® Model B (W.S. Tyler Incorporated). The particle size distribution was measured using a Beckman Coulter LS 13–320 static light scattering analyzer by suspending the particles in DI water. The particle size distribution was used to calculate the geometric surface area (GSA) in cm^2/g of the samples as [30].

$$GSA = \sum_{i=1}^n \frac{SA_i \varphi_i}{V_i \rho_{slag}} \quad (1)$$

where φ_i is the volume fraction of particles with diameters between d_i and d_{i+1} while SA_i (in cm^2), and V_i (in cm^3) are the surface area and volume of the spherical particle, respectively. The density of the slag ρ_{slag} was taken as 3.46 g/cm^3 [31].

The mineralogical composition of the BOF slag was determined prior to and after 30 min of dissolution using X-ray diffraction (XRD). XRD analysis was performed using a PANalytical X'Pertpro diffractometer (θ - θ configuration, $\text{CuK}\alpha$ radiation, $\lambda = 1.54 \text{ \AA}$). Scans were acquired between 5° and 70° with a step scan of 0.02° using a scientific X'Celerator 2 detector on powder samples. Finally, the chemical composition (in mass %) of the BOF slag was measured using X-ray fluorescence (XRF). The slag was dominantly composed of Fe_2O_3 (65.9%), followed by CaO (19.3%), SiO_2 (7.1%), MgO (4.7%), and Al_2O_3 (1.71%). The results are in accordance with literature [32,33]. This information was used to quantify the calcium leaching yield (or extraction) X_{Ca} from the slag to the leaching solution according to $X_{\text{Ca}} = n_{\text{Ca,sln}}(t = 30 \text{ min}) / n_{\text{Ca,slag}}$ where $n_{\text{Ca,sln}}(t = 30 \text{ min})$ are the number of moles of calcium in solution after 30 min of leaching and $n_{\text{Ca,slag}}$ are the number of moles of calcium in the solid slag as measured by XRF.

2.1.2. $\text{Ca}(\text{OH})_2$ characterization

The total mass of $\text{Ca}(\text{OH})_2$ precipitated experimentally $m_{\text{Ca}(\text{OH})_2,e}$ was

determined as the sum of $\text{Ca}(\text{OH})_2$ recovered in the filter bags and that precipitated on the surface of the heaters of the precipitation reactor. At the end of the experiment, the precipitated $\text{Ca}(\text{OH})_2$ was collected, weighed, and stored under vacuum conditions at room temperature for one week for subsequent analysis. The mass of $\text{Ca}(\text{OH})_2$ remaining on the filters was determined by subtracting the mass of the filters dried at 60°C for 24 h from the initial mass of the unused filter. The mass production rate $\dot{m}_{\text{Ca}(\text{OH})_2,e}$ of $\text{Ca}(\text{OH})_2$ was estimated as the mass of $\text{Ca}(\text{OH})_2$ measured experimentally divided by the duration of the experiment.

The $\text{Ca}(\text{OH})_2$ crystals were characterized using thermogravimetric analysis (TGA), X-ray diffraction (XRD), and scanning electron microscopy (SEM). TGA measurements were performed using a Perkin Elmer STA 6000. First, the sample was equilibrated at 35°C for 5 min to establish a mass baseline. Then, the sample was gradually heated from 35°C to 900°C at a rate of $10^\circ\text{C}/\text{min}$ while continuously monitoring the mass. Ultra-high purity N_2 gas was circulated through the sample chamber at a flow rate of 20 mL/min. The mass change versus temperature revealed the presence and quantity of H_2O , $\text{Ca}(\text{OH})_2$ and CaCO_3 present on account of their characteristic thermal decomposition at temperatures in excess of $\sim 100^\circ\text{C}$, $\sim 400^\circ\text{C}$ [34,35] and $\sim 600^\circ\text{C}$ [36], respectively. XRD analysis was performed as previously detailed for the slag characterization. Here, portlandite PDF #04-010-3117 was used as a reference. Finally, the morphology of the vacuum-dried crystals was evaluated using a G2 Phenom scanning electron microscope fitted with an energy dispersive (SEM-EDS) X-ray analyzer under high vacuum conditions at an accelerating voltage of 15 kV.

2.2. Pilot system

2.2.1. Equipment

Fig. 1 shows (a) a schematic rendering and (b) a photograph of the experimental pilot system built to produce $\text{Ca}(\text{OH})_2$. A video of the operation of the pilot system is presented in [supplementary information](#). The three main unit operations were (i) leaching (batch operation), (ii) concentration by reverse osmosis (continuous operation), and (iii) precipitation (continuous operation). Leaching was carried out in a stirred leaching reactor comprised of a polyethylene cone tank (150 L) stirred by a Dayton drum mixer operating at 1700 rpm. Thereafter, two separation steps were used to remove the solids from the leachate. First, a trap for solid particulates (Gleco trap HV, 18 L capacity) was placed at the exit of the leaching reactor to separate the coarser grains of slag from the leachate. Second, a cartridge filter was placed at the exit of the leachate buffer tank to prevent particles larger than $5 \mu\text{m}$ from entering the feed reservoir. Each leachate batch was discharged to the leachate buffer tank (160 L) using a centrifugal pump (Iwaki NRD series) with 900 L/h capacity. A gear pump (micropump GJ series) was used to maintain a constant flow rate of solution from the leachate buffer to the feed reservoir and enabled the coupling of the batch leaching step with the continuous concentration and precipitation steps of the process.

Reverse osmosis concentration was performed by pressurizing the feed – with a Goulds pump (1SV30FF4C60) connected to an Aquavar intelligent pump controller – through two pressure vessels operating in series equipped with BW30–2540 Filmtec spiral wound membranes (5.2 m^2 total active membrane area). To minimize the water consumption, the permeate stream was recycled for leaching. Using the permeate buffer tank (160 L), the permeate stream was collected until the tank was full. Subsequent leaching batches were carried out using the permeate solution collected in the mentioned buffer tank by quickly transferring the permeate to the leaching tank using a submersible pump. Thus, the water was fully recirculated and the process was sustained using only the water required to startup the system. The retentate stream was directed to a thermally insulated stainless-steel precipitation reactor ($V_{\text{precip}} = 190 \text{ L}$) operating at a constant temperature of $95 \pm 5^\circ\text{C}$ maintained with two 6 kW Tempco electric heaters. Mixing in the precipitation reactor was achieved by using an electric mixer operating

Table 1
Operating conditions used to test the system during the pilot tests 1, 2, and 3.

Operating parameters for Pilot test #:	1	2	3
Average feed flow rate \dot{V}_F (L/h)	254	185	90
Average saturate flow rate \dot{V}_S (L/h)	134	90	44
Average leachate flow rate \dot{V}_L (L/h)	120	95	46
Hours of continuous operation (h)	8	12	24
Average precipitation temperature T_S (°C)	87	95	95

at 1750 rpm. After precipitation, the $\text{Ca}(\text{OH})_2$ crystals were collected by pumping the saturated solution through a filter bag (pore size: 5 μm) with stainless steel housing. Thereafter, the filtered saturated solution was recycled back to the feed reservoir and mixed with the leachate stream. A copper coil placed inside the feed reservoir (1.3 m^2 heat exchange area) was used for cooling the feed stream by circulating 450 L/h of water at 18 °C.

2.2.2. Instrumentation and sampling

The temperatures in the feed reservoir and in the precipitation reactor were continuously monitored using two Type-T thermocouples connected to a data acquisition card (NI-9213 connected to a NI USB-9162) and recorded using Labview V14. The pressure in the retentate stream and the conductivity in the feed reservoir were continuously measured using a data acquisition card Iotech DAQ 3000 Series using DasyLab V10 connected to a Balluff pressure sensor and a conductivity meter (Omega CDTX-2853), respectively. The conductivity measurements were used to estimate the calcium concentration of the feed stream using a calibration curve relating conductivity to the total calcium concentration $[\text{Ca}]$ (Fig. S1). During continuous operation, the flow rates in the permeate, retentate, saturate, and leachate streams were recorded every hour using analog King flowmeters. In addition, 20 mL samples were taken every hour in each stream to measure the concentration of dissolved species. Additionally, solution aliquots of 20 mL were extracted after 0, 5, 10, 20, and 30 min for every leaching batch. All samples were immediately filtered through 0.2 μm syringe filters to remove particulates and to avoid concentration changes in the sample. Analysis of the total dissolved calcium concentration $[\text{Ca}]$ was performed using a Perkin Elmer Avio 200 inductively coupled plasma – optical emission spectrometer (ICP-OES). Prior to elemental analysis, the samples were diluted in 5 vol% HNO_3 . The ICP-OES was calibrated using standard solutions containing calcium in concentrations of 0, 0.1, 1, 10, 25, 50, and 100 ppm prepared using analytical (1000 ppm) standards procured from Inorganic Ventures.

2.2.3. Startup procedure and operating conditions

During the startup, 7.5 kg of BOF slag were mixed with 150 L of water for 30 min to achieve a solid to liquid mass fraction (s/l) of 0.05 and $[\text{Ca}]$ concentration of ~ 11 mM. Four leaching batches were used to

fill the feed reservoir (300 L) and the leachate buffer tank with the leachate solution. Subsequently, the precipitation reactor was filled with concentrated leachate solution and heated to 95 °C. After the concentrated leachate achieved the desired temperature, the pumps feeding and draining the feed reservoir were turned on for continuous operation. Additionally, during continuous operation, the s/l ratio for leaching was switched from 0.05 to 0.03 to maintain a constant feed concentration $[\text{Ca}]_F$ of 10 mM and to minimize slag consumption.

The pilot was tested in continuous operation in 8, 12, and 24-hour trials, herein referred to as pilot test 1, 2, and 3, respectively. Table 1 shows the operating conditions of the three pilot tests. Different feed pressure and flow rates were tested to evaluate changes in the process and characteristics of the final product.

2.3. Energy balance

To perform a detailed energy balance of the process, the energy of grinding and mixing as well as the energy consumed for heating and pumping were calculated as follows.

Grinding energy consumption: The specific energy consumption of grinding slag $w_{g,slag}$ (in kWh/ton slag) was given by [37].

$$w_{g,slag} = W_b \left(\frac{10}{\sqrt{d_f}} - \frac{10}{\sqrt{d_i}} \right) \quad (2)$$

where $W_b = 18.3$ kWh/ton slag is the Bond work index of slag [38], $d_i = 9500$ μm is the initial particle size, and $d_f = 100$ μm is the desired final particle size. The energy associated with grinding was given by $W_g = w_{g,slag} m_{slag}$ where the total mass of slag m_{slag} used was 48 kg, 50.5 kg, and 59.5 kg, for pilot tests 1, 2, and 3, respectively. The specific grinding energy consumption (per unit mass of $\text{Ca}(\text{OH})_2$) was calculated by dividing the grinding energy by the total mass of $\text{Ca}(\text{OH})_2$ produced, i.e., $w_g = W_g / m_{\text{Ca}(\text{OH})_2, e} = w_{g,slag} m_{slag} / m_{\text{Ca}(\text{OH})_2, e}$.

Mixing energy consumption: The power consumption of the mixers \dot{W}_m (in W) was computed according to [39].

$$\dot{W}_m = N_p \rho \omega^3 D_I^5 \quad (3)$$

where $N_p = 0.35$ is the power number, $\rho = 1000$ kg/m^3 is the density of water, $\omega = 29$ s^{-1} is the rotation frequency (corresponding to a standard 1750 rpm electric motor), and $D_I = 0.095$ m is the impeller diameter [39]. Each leaching batch was stirred for 30 min (or 1800 s). Thus, the energy consumed by the mixer during leaching $W_{m,L}$ (in J) was expressed as

$$W_{m,L} = 1800 N_b \dot{W}_m \quad (4)$$

where N_b is the total number of leaching batches carried out during the experiments. Pilot tests 1, 2, and 3 consumed $N_b = 7, 9,$ and 11 leaching

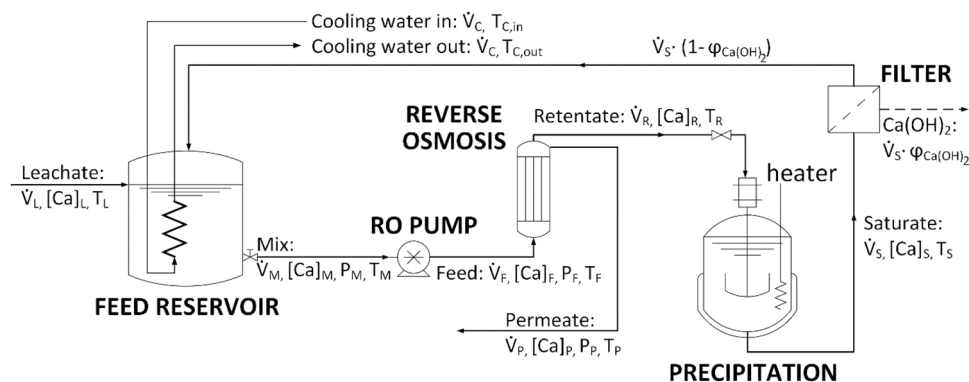


Fig. 2. Process flow diagram of the steady-state model to produce $\text{Ca}(\text{OH})_2$ from alkaline calcium-containing leachates. The variables considered in the model include the volumetric flow rate \dot{V} , the calcium concentration $[\text{Ca}]$, the pressure P , and the temperature T in each unit operation.

batches, respectively. The factor 1800 corresponds to the duration (in s) of each leaching batch. The mixer used in the stirred precipitation reactor was continuously active during the entire process. Thus, the mixing energy consumption of the continuously stirred precipitation reactor was given by

$$W_{m,P} = \tau \dot{W}_m \quad (5)$$

where τ is the duration of the pilot test (in s) corresponding to 8, 12, and 24 h for pilot tests 1, 2, and 3, respectively.

The total energy consumed by the mixers in the entire process W_m (in J) was expressed as

$$W_m = W_{m,L} + W_{m,P} \quad (6)$$

The specific mixing energy consumption (per unit mass of Ca(OH)_2) was computed by dividing the mixing energy by the total mass of Ca(OH)_2 produced: $w_m = W_m / m_{\text{Ca(OH)}_2, e}$.

3. Modeling

3.1. Assumptions

To design the pilot system, a steady-state model of the process was developed based on mass and energy conservation principles and validated using Aspen Plus v10 (Fig. S2) [40]. Fig. 2 shows the process flow diagram of the model and the variables considered in each unit operation. The leaching process was not simulated because the rate and magnitude of calcium release from the slag could be influenced by many factors such as the type of slag, the particle size, the solid to liquid mass fraction (s/l), and the type of leaching reactor, e.g., batch, plug flow, continuously stirred reactor [24,25,41]. Instead, the leachate concentration $[\text{Ca}]_L$ was imposed to generalize the process to any type of alkaline leachate.

The model was based on the following assumptions: (i) the process operated at steady state. (ii) The fluid was incompressible. (iii) The solution density was independent of temperature and was approximated as that of water. (iv) The leachate entered the feed reservoir with a leachate calcium concentration $[\text{Ca}]_L$ at flow rate \dot{V}_L . (v) The water was fully recirculated, i.e., $\dot{V}_L = \dot{V}_p$. (vi) The temperature, pressure, and concentration were uniform inside each unit operation. (vii) The complexation of calcium ions in solution was ignored and calcium was present either as Ca^{2+} ions and hereafter referred to as $[\text{Ca}]$ or as solid Ca(OH)_2 according to the precipitation reaction $\text{Ca}^{2+} + 2\text{OH}^- \leftrightarrow \text{Ca(OH)}_{2(s)}$.

3.2. Model governing equations

Pump: The power delivered by the RO pump \dot{W}_p to increase the pressure of the solution from atmospheric pressure ($P_M = 101,325$ Pa) in the feed reservoir to the desired feed stream pressure P_F entering the RO unit was defined as [42]

$$\dot{W}_p = \frac{\dot{V}_F (P_F - P_M)}{\eta_p} \quad (7)$$

where \dot{V}_F is the volumetric flow rate of the feed solution and $\eta_p = 0.8$ is the hydraulic efficiency of the pump. Here also, the specific pumping energy w_p (in J/kg of Ca(OH)_2) was calculated by dividing the pumping power by the Ca(OH)_2 production rate, i.e., $w_p = \dot{W}_p / \dot{m}_{\text{Ca(OH)}_2}$.

Reverse Osmosis (RO) unit: To model the RO membrane separation step, the mass conservation equations for the solution and the calcium were expressed, respectively, as

$$\dot{V}_F = \dot{V}_P + \dot{V}_R \quad (8)$$

$$\dot{V}_F [\text{Ca}]_F = \dot{V}_P [\text{Ca}]_P + \dot{V}_R [\text{Ca}]_R \quad (9)$$

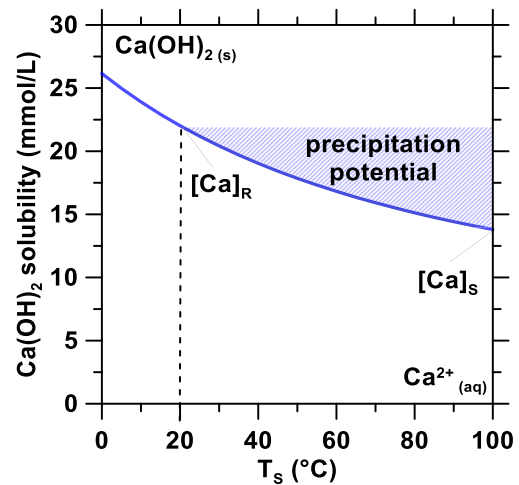


Fig. 3. Ca(OH)_2 solubility in water as a function of temperature T_s [28].

where \dot{V}_F , \dot{V}_P , and \dot{V}_R are the volumetric flow rates (in m^3/s) of the feed, permeate, and retentate streams, respectively. Similarly, $[\text{Ca}]_F$, $[\text{Ca}]_P$, and $[\text{Ca}]_R$ (in mol/m^3) are the calcium concentrations of the feed, permeate, and retentate streams, respectively. The volumetric flow rate of the permeate stream was given by [43]

$$\dot{V}_P = A_m L_p (\Delta P_{mem} - \Delta\pi) \quad (10)$$

where $A_m = 5.2$ m^2 is the membrane area, $L_p = 8.64 \times 10^{-12}$ $\text{m}^3/(\text{s m}^2 \text{ Pa})$ is the membrane permeability estimated from experimental data [17] and matching that reported in literature [44–46]. The transmembrane pressure difference ΔP_{mem} is defined as the difference between the feed P_F and the permeate P_P pressures, i.e., $\Delta P_{mem} = P_F - P_P$. The permeate stream was assumed to be at atmospheric pressure ($P_P = 101,325$ Pa). The osmotic pressure difference between the feed and the permeate solutions was computed according to [43,47]

$$\Delta\pi = R_U T_F [([\text{Ca}]_F + [\text{OH}^-]_F) - ([\text{Ca}]_P + [\text{OH}^-]_P)] \quad (11)$$

where $R_U = 8.314$ $\text{J}/\text{mol}\cdot\text{K}$ is the universal gas constant and $T_F = 293$ K is the feed solution temperature. The concentration of hydroxide ions $[\text{OH}^-]$ in the entire process was calculated based on the electroneutrality principle such that $2[\text{OH}^-] = [\text{Ca}]$. The permeate calcium concentration $[\text{Ca}]_P$ was calculated based on the membrane rejection coefficient $R = 0.99$ according to the membrane manufacturer so that

$$[\text{Ca}]_P = [\text{Ca}]_F (1 - R) \quad (12)$$

Precipitation: Following concentration in the RO unit, the retentate solution entered a continuously stirred precipitation reactor. The solution in this unit was assumed to be in equilibrium with the solid portlandite, i.e., $\text{Ca}^{2+} + 2\text{OH}^- \leftrightarrow \text{Ca(OH)}_{2(s)}$. The saturation concentration $[\text{Ca}]_s$ was calculated based on the solubility of portlandite as a function of temperature $[\text{Ca}]_s = f(T_s)$, plotted in Fig. 3. The volume flow rate of solid Ca(OH)_2 exiting the crystallizer $\dot{V}_{\text{Ca(OH)}_2}$ was expressed as

$$\dot{V}_{\text{Ca(OH)}_2} = \dot{V}_s \varphi_{\text{Ca(OH)}_2} = \dot{V}_s \frac{M_{\text{Ca(OH)}_2} ([\text{Ca}]_R - [\text{Ca}]_s)}{\rho_{\text{Ca(OH)}_2}} \quad (13)$$

where \dot{V}_s is the saturate flow rate and $\varphi_{\text{Ca(OH)}_2} = \dot{V}_{\text{Ca(OH)}_2} / \dot{V}_s$ is the volume fraction of Ca(OH)_2 in the saturated solution. Here, $\rho_{\text{Ca(OH)}_2} = 2.2$ kg/m^3 is the density of Ca(OH)_2 , $M_{\text{Ca(OH)}_2} = 0.074$ kg/mol is the molar mass of Ca(OH)_2 and $[\text{Ca}]_R$ and $[\text{Ca}]_s$ are the retentate and saturate total calcium concentrations, respectively. The mass flow rate of Ca(OH)_2 was calculated as $\dot{m}_{\text{Ca(OH)}_2} = \rho_{\text{Ca(OH)}_2} \dot{V}_{\text{Ca(OH)}_2}$. Since the volume fraction of Ca(OH)_2 is very small $\varphi_{\text{Ca(OH)}_2} \sim 2.6 \times 10^{-4}$ the volumetric

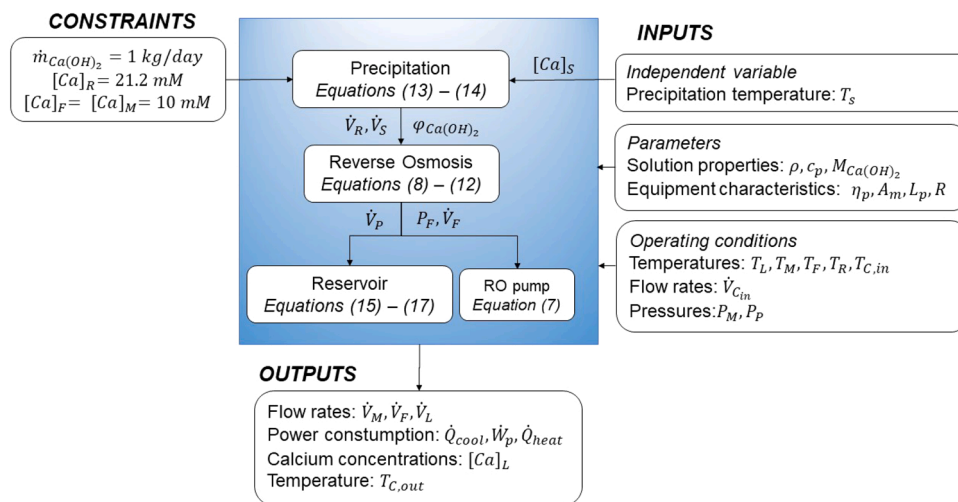


Fig. 4. Block diagram of the solution method to predict the heat and power consumption of the Ca(OH)_2 production process for a rate of 1 kg per day.

flow rate of the retentate and saturated stream were assumed to be equal so that $\dot{V}_R = \dot{V}_S$. Now, the thermal power (in W) required for Ca(OH)_2 precipitation was written as

$$\dot{Q}_{heat} = \rho c_p \dot{V}_R (T_S - T_R) \quad (14)$$

where $\rho = 1000 \text{ kg/m}^3$ and $c_p = 4184 \text{ J/kg}\cdot\text{K}$ are respectively the density and heat capacity of the solution, taken as those of water [48], while T_S and T_R are saturate and retentate temperatures, respectively. The

retentate temperature T_R was assumed to be constant at 20°C . The precipitation temperature T_S was treated as an independent variable. The specific thermal energy q_{heat} [in J/kg Ca(OH)_2] consumed during the precipitation process was calculated by dividing the heating power \dot{Q}_{heat} by the Ca(OH)_2 mass production rate, i.e., $q_{heat} = \dot{Q}_{heat} / \dot{m}_{\text{Ca(OH)}_2}$. Due to the low solubility of Ca(OH)_2 in water, the saturate calcium concentration $[\text{Ca}]_S$ is expected to be on the order of 14 – 16 mM. Thus, to maximize the conversion of aqueous calcium into solid Ca(OH)_2 , the saturated solution was recirculated back to the feed reservoir.

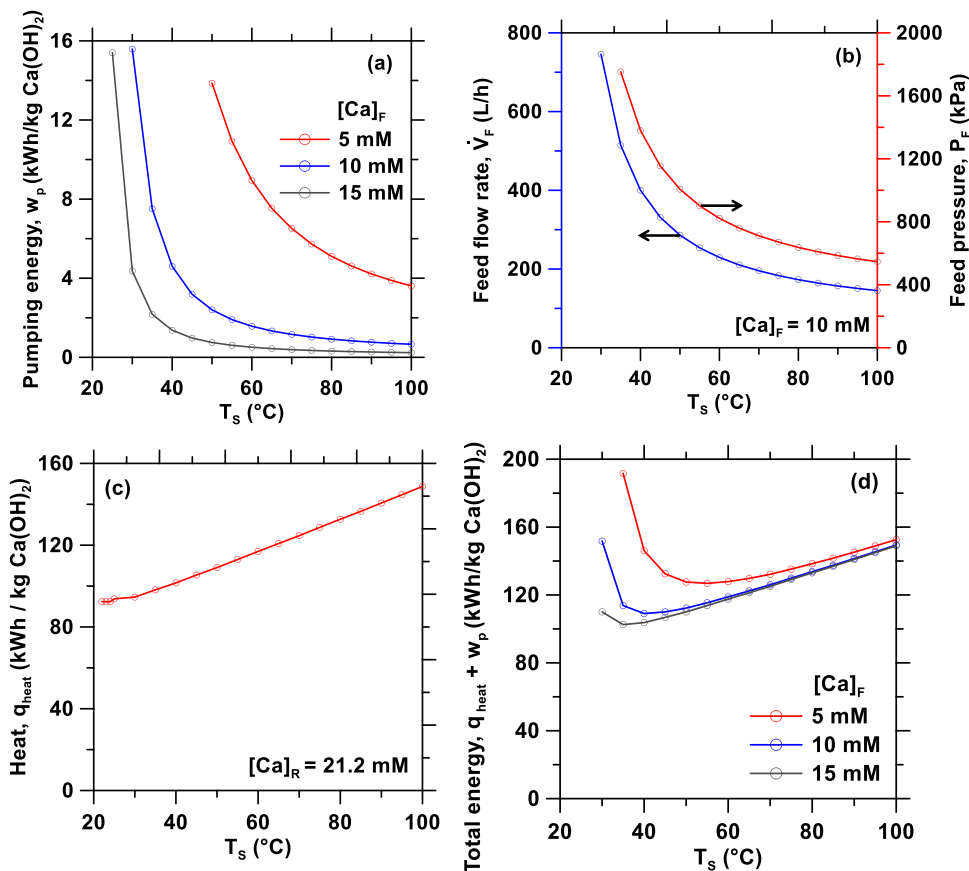


Fig. 5. Predicted (a) specific pumping power consumption, (b) feed flow rate \dot{V}_F and pressure P_F for a fixed feed $[\text{Ca}]_F$ concentration of 10 mM, (c) specific heat consumption q_{heat} , and (d) total specific energy consumption $q_{heat} + w_p$ as functions of precipitation temperature assuming retentate $[\text{Ca}]_R$ concentration of 21.2 mM so as to produce 1 kg of Ca(OH)_2 per day.

Feed Reservoir: The mass conservation equations for the solution and calcium in the feed reservoir can be written as

$$\dot{V}_M = \dot{V}_L + \dot{V}_S [1 - \varphi_{Ca(OH)_2}] \quad (15)$$

$$\dot{V}_M [Ca]_M = \dot{V}_L [Ca]_L + \dot{V}_S [1 - \varphi_{Ca(OH)_2}] [Ca]_S \quad (16)$$

where \dot{V}_M , \dot{V}_L , and \dot{V}_S are the volumetric flow rates, and $[Ca]_M$, $[Ca]_L$, and $[Ca]_S$ are the calcium concentrations of the mixed, leachate, and saturate streams, respectively. The energy required to have a mix stream temperature T_M of 20 °C was expressed as [48]

$$\begin{aligned} \dot{Q}_{cool} &= \rho c_p \dot{V}_M \left(T_M - \frac{\dot{V}_L T_L + \dot{V}_S (1 - \varphi_{Ca(OH)_2}) T_S}{\dot{V}_L + \dot{V}_S (1 - \varphi_{Ca(OH)_2})} \right) \\ &= \rho c_p \dot{V}_C (T_{C,out} - T_{C,in}) \end{aligned} \quad (17)$$

where \dot{V}_C is the flow rate, and $T_{C,in}$ and $T_{C,out}$ are the inlet and outlet temperatures of the water cooling the reservoir. The cooling power \dot{Q}_{cool} and the operating constraints of the pilot system - with cooling stream flow rate $\dot{V}_C = 454$ L/h, and inlet temperature $T_{C,in} = 18$ °C - were used to design the heat exchanger area necessary to cool the actual feed reservoir using the countercurrent heat exchanger model [48].

3.3. Method of solution

Fig. 4 shows a block diagram of the solution method used to calculate the power consumption and the heating and cooling requirements to produce 1 kg of $Ca(OH)_2$ per day with the proposed three-step process. The model was initialized and solved by simple substitution based on the design constraints of the pilot system. Model validation was performed by comparing the results with those of Aspen Plus V10.

The constraints used to initialize the model were (i) a $Ca(OH)_2$ production rate $\dot{m}_{Ca(OH)_2}$ of 1 kg per day, (ii) a retentate concentration $[Ca]_R$ of 21.2 mM, and (iii) a feed concentration $[Ca]_F$ of 10 mM. Then, the model was used to identify the influence of precipitation temperature and feed calcium concentration on the water consumption, and heating and pumping requirements of the process. The operating conditions of the experimental pilot process were optimized to minimize the pumping power of the RO-driven concentration since the electricity consumption of this step contributed significantly to the operating cost of the process. The overall energy consumption as a function of precipitation temperature was also evaluated, but the results were not used to guide the operation of the pilot system since the waste heat required for precipitation should be available from thermal power plants at low or no cost.

4. Results and discussion

4.1. Modeling the effect of different operating conditions on power consumption

Fig. 5 shows the model predictions for (a) the specific pumping power consumption w_p , (b) the feed flow rate \dot{V}_F and pressure P_F , (c) the specific heat consumption q_{heat} , and (d) the total specific energy consumption $q_{heat} + w_p$ as functions of the precipitation temperature T_S to achieve a retentate concentration $[Ca]_R$ of 21.2 mM and a mass production rate $\dot{m}_{Ca(OH)_2}$ of 1 kg of $Ca(OH)_2$ per day. Fig. 5(a) indicates that the specific pumping energy consumption to drive the RO unit decreased exponentially with increasing precipitation temperature T_S . Because of the decreasing solubility of $Ca(OH)_2$ with increasing temperature, lower feed solution flow rate \dot{V}_F and pressure P_F were needed as the precipitation temperature increased [Fig. 5(b)]. In addition, increasing the feed concentration $[Ca]_F$ to 15 mM further reduced the pumping energy w_p and the feed pressure P_F since a smaller degree of concentration was

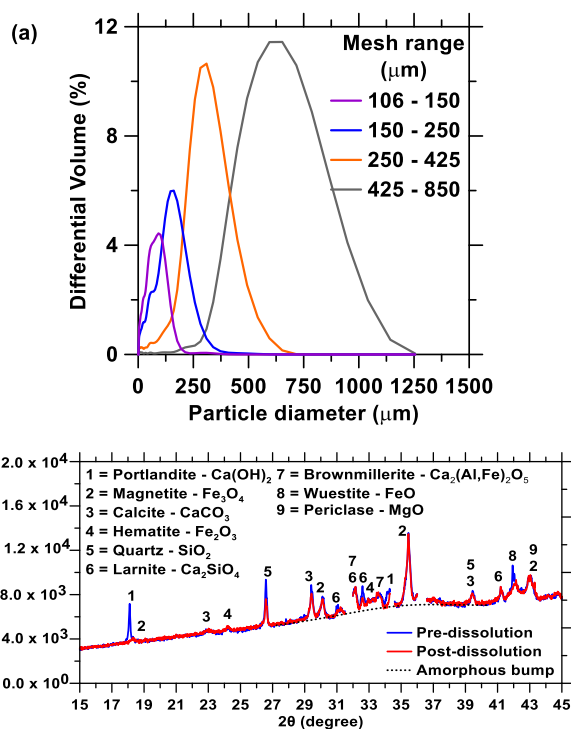


Fig. 6. (a) particle size distribution of the slag and (b) XRD diffractogram of the slag before and after 30 min of dissolution in DI water. The results indicate that $Ca(OH)_2$ dissolution was predominant over any other phases present in the slag. Note that the discontinuity in the diffractogram at 31.7°, 34.4°, and 36.2° 2θ correspond to zincite (ZnO , 99.999%) peaks that were cut off for clarity. ZnO was used as an internal standard for XRD analysis to determine the amount of amorphous slag.

necessary to achieve the saturation point of portlandite in the retentate ($[Ca]_R = 21$ mM). However, this scenario might not be realistic considering that slag typically yields leachate calcium concentration $[Ca]_L$ below 10 mM. Nevertheless, it could be relevant when leaching other alkaline wastes or minerals.

As expected, Fig. 5(c) shows that the thermal energy q_{heat} required per kg of $Ca(OH)_2$ precipitate increased quasi-linearly as the precipitation temperature T_S increased. Finally, Fig. 5(d) shows the total specific energy consumption is minimum when operating the precipitation reactor at T_S in the range of 40–55 °C, depending on the feed concentration. Below 40 °C, pumping requirements superseded thermal energy input. Above 55 °C, the decrease in pumping energy consumption was marginal, and the heat consumption dominated. For upscaling purposes, operating around 40–55 °C is desirable as a large fraction of the waste heat in thermal power plants comes from condensers and is typically below 50 °C [49]. Moreover, the yield of $Ca(OH)_2$ precipitated per liter of solution and the specific RO pumping energy could be enhanced by operating the feed and retentate streams at ~5 or 10 °C to achieve larger concentration difference between the retentate $[Ca]_R$ and saturate $[Ca]_S$ streams. However, to demonstrate the continuous pilot process, we chose to operate the precipitation step at temperature $T_S = 95$ °C to minimize electricity consumption for the RO pump and to maximize $Ca(OH)_2$ production throughput.

4.2. Slag leaching

4.2.1. Insights in the dissolution of BOF slag in DI water

Fig. 6(a) shows the particle size distribution of the slag. Fig. 6(b) shows the XRD patterns of BOF slag before and after dissolution. The following crystalline phases were detected in the slag before dissolution: portlandite - $Ca(OH)_2$ (PDF #04-010-3117), quartz - SiO_2 (PDF

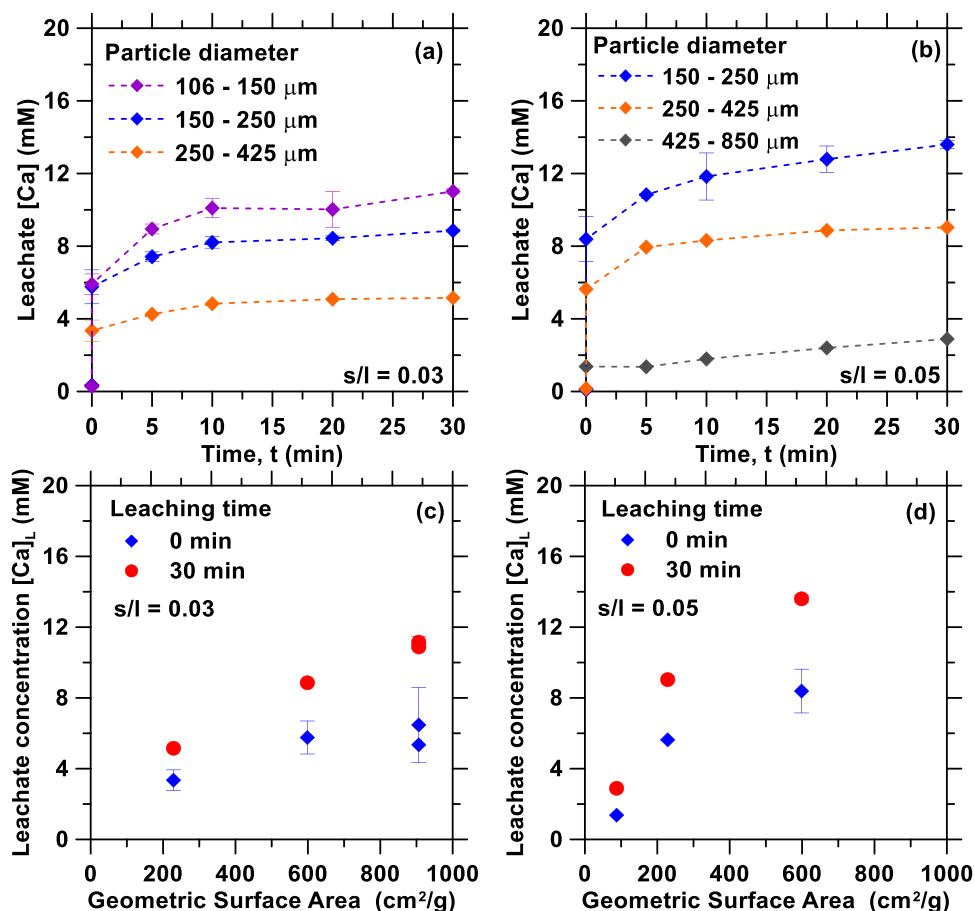


Fig. 7. Leachate concentration $[Ca]_L$ as a function of time and particle size fraction for a solid to liquid ratio (s/l) of (a) 0.03 and (b) 0.05. Initial ($t = 0$ min) and final ($t = 30$ min) leachate calcium concentration $[Ca]_L$ as a function of geometric surface area for a s/l ratio of (c) 0.03, and (d) 0.05.

#04-012-0490), calcite – CaCO_3 (PDF #04-008-0788), larnite – Ca_2SiO_4 (AMCSD #0020214), brownmillerite – $\text{Ca}_2(\text{Fe,Al})_2\text{O}_5$ (AMCSD # 0003434), wüstite – FeO (AMCSD #0002758), periclase – MgO (PDF #04-010-4039), magnetite – Fe_3O_4 (PDF #04-005-4319), and hematite – Fe_2O_3 (PDF #04-003-2900). All these crystalline phases are commonly found in BOF slag [32,33].

Fig. 6 indicates a complete dissolution of the slag portlandite content, whereas the other crystalline phases present in the slag were nearly undissolved after 30 min of leaching. Moreover, the broad amorphous peak intensity in XRD did not present significant differences before and after dissolution, indicating that the amorphous content of the slag was nearly insoluble. Thus, the results indicated that $\text{Ca}(\text{OH})_2$ was the main source of calcium dissolved from slag. This was further confirmed by elemental analysis of the leachates showing that the concentrations of silicon, aluminum, sodium, and iron were at least one order of magnitude lower than the final concentration of calcium (see Fig. S3 in Supplementary material). This observation was consistent with the lower solubility and/or kinetic rate constant of the other phases present in slag compared to portlandite [25]. Typically, BOF slag is underutilized in the construction industry compared to other types of slag because its high free lime content may generate cracking in concrete [50,51]. This high free lime content was ideal for the present application, since larger calcium concentrations were leached from BOF slag than from other types of slag in DI water [17].

4.2.2. Effect of particle size distribution on leachate calcium concentration

Fig. 7 shows the leachate concentration $[Ca]_L$ achieved experimentally as a function of time for a solid to liquid (s/l) ratio of (a) 0.03 and (b) 0.05. It also plots the initial ($t = 0$ min) and final ($t = 30$ min)

leachate calcium concentration $[Ca]_L$ as a function of geometric surface area for a s/l ratio of (c) 0.03, and (d) 0.05. Fig. 7(a) and 7(b) indicate that calcium leaching was fast initially followed by a slower release after 10 min. The monotonic increase of $[Ca]_L$ for all s/l ratios and particle sizes considered indicated that little to no hydrated phases precipitated during slag dissolution. Indeed, if other calcium phases had precipitated, the dissolved calcium in solution would have decreased eventually [17]. Fig. 7(c) and 7(d) show that, as the geometric surface area increased, the initial leachate concentration $[Ca]_L$ (at 0 min) approached a similar value of ~ 8 mM for both s/l ratios considered. Additionally, Fig. 7(c) and 7(d) reveal that the leachate concentration $[Ca]_L$ difference between 0 and 30 min increased with increasing geometric surface area. In other words, increasing the geometric surface area increased the dissolution rate [52].

Decreasing the particle size and the leaching time seems more desirable than increasing the s/l ratio to maximize the calcium conversion during leaching while minimizing raw material consumption. Indeed, increasing the s/l ratio while maintaining the same particle size did not have a significant effect on Ca leaching yield X_{Ca} . However, decreasing the particle size increased the yield X_{Ca} from 5% to 11% and from 2% to 8% for s/l ratios of 0.03 and 0.05, respectively. However, decreasing the particle size may also increase other species dissolution and specifically the Si-containing amorphous fraction [52,53]. This could lead to an increase of Si content in solution which could result in the formation of C-S-H phases instead of $\text{Ca}(\text{OH})_2$. Thus, further experiments with smaller slag particle size should be evaluated to find the optimum leaching conditions where portlandite dissolution is maximized and dominates over the dissolution of other phases in the slag. In practice, the Ca leaching yield could be improved by using a semi-batch

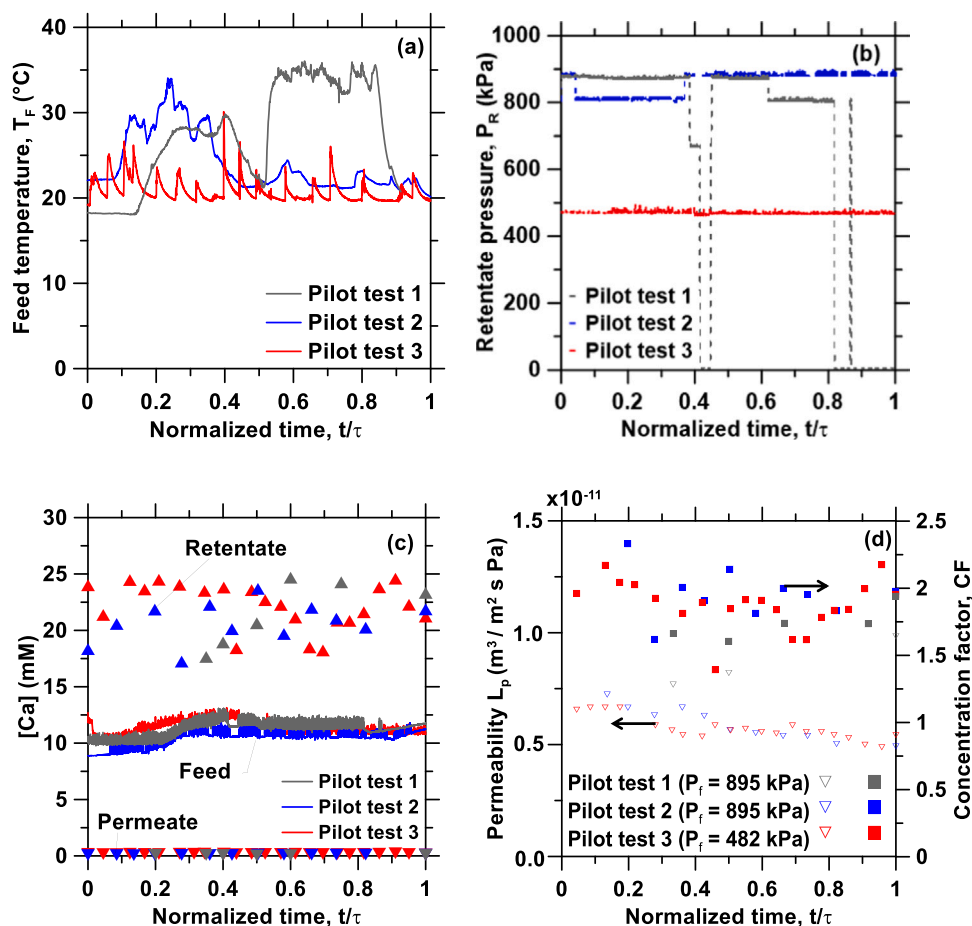


Fig. 8. (a) Feed temperature, (b) retentate pressure, (c) [Ca] concentration in the feed, retentate and permeate streams, and (d) Membrane permeability and concentration factor as functions of time.

or continuous process based on a series of countercurrent leaching vessels and/or by increasing the leaching time to maximize calcium dissolution. Moreover, when increasing the leaching time to maximize calcium dissolution, the stirring energy required for the leaching process should be minimized.

4.3. Stability of reverse osmosis concentration

The slag leachate solutions were concentrated continuously through the RO unit at a constant water recovery ratio of 0.52 to achieve similar concentration factors in all tests. Fig. 8 shows the measured (a) feed temperature T_F , (b) retentate pressure P_R , (c) total calcium concentrations in the feed $[Ca]_F$, retentate $[Ca]_R$ and permeate $[Ca]_P$ streams, as well as (d) membrane permeability L_p and concentration factor ($CF = [Ca]_R/[Ca]_F$) as functions of time. Fig. 8(a) indicates that the feed temperature ranged from 20 °C to 30 °C in all the experiments, indicating that the cooling system functioned properly. Fig. 8(b) shows that the pressure drop ($P_F - P_R$) across the RO system between the feed and retentate was 15 kPa for pilot tests 1 and 2. Pilot test 3 operated at a slightly lower pressure drop of 12 kPa due to the lower feed flow rate. Fig. 8(c) indicates that the feed concentration $[Ca]_F$ was constant around 10 ± 2 mM, as expected from the process design. The permeate concentration $[Ca]_P$ remained below 1 mM suggesting negligible membrane degradation. This was confirmed by the calcium rejection averaging 99.3%, 99.1% and 98.7% in pilot tests 1, 2, and 3, respectively.

Fig. 8(d) indicates that the concentration factor CF was around 2 for all tests performed and operated at the same water recovery ratio of 0.52. Additionally, it shows that membrane permeability [Eq. (4)] decreased as a function of time, probably due to fouling or scaling. The

decrease in membrane permeability L_p was more prominent during the first 8 h of continuous operation. This could be due to membrane compaction and system equilibration [54]. Additionally, the decrease in membrane permeability L_p was larger at higher feed pressure namely 43% at 895 kPa in pilot test 2, compared to 10% at 482 kPa in pilot test 3. This observation can be attributed to the stronger convective force of the permeate passing through the membrane at larger pressures resulting in membrane fouling [55]. After each test, the membrane was cleaned with a diluted nitric acid solution (pH ~ 3) for 1 h. The cleaning procedure improved the permeability, demonstrating that fouling can be reversed. Although the BW30–2540 membranes used in the pilot test are not designed to operate at pH larger than 11, the membranes remained stable while operating at a pH of 12.4 in the three tests performed. Nevertheless, study of membrane durability should be performed for different commercially available products before upscaling the technology to select the most suitable RO membrane.

Fig. 8(c) and 8(d) show the calcium concentration $[Ca]_R$ and the concentration factor CF in the retentate as functions of time, respectively. Since $[Ca]_R$ was always above 15 mM, the solution entering the precipitation reactor was always supersaturated with $\text{Ca}(\text{OH})_2$ when heated at 90 °C. On average, $[Ca]_R$ was 21.6, 20.7, and 22.2 mM for pilot tests 1, 2 and 3, respectively. Fig. 8(c) and 8(d) indicate that the membranes tolerated calcium containing solutions concentrated above the saturation point of $\text{Ca}(\text{OH})_2$ since its permeability was very similar in all cases. Nevertheless, Fig. 8(d) shows that a decrease in concentration factor coincided with an improvement in membrane permeability (for example at normalized time t/τ of 0.45 and 0.7 in pilot test 3), indicating that the permeability decline could be due to scale formation. However, it could be reversed when the retentate concentration $[Ca]_R$ decreased.

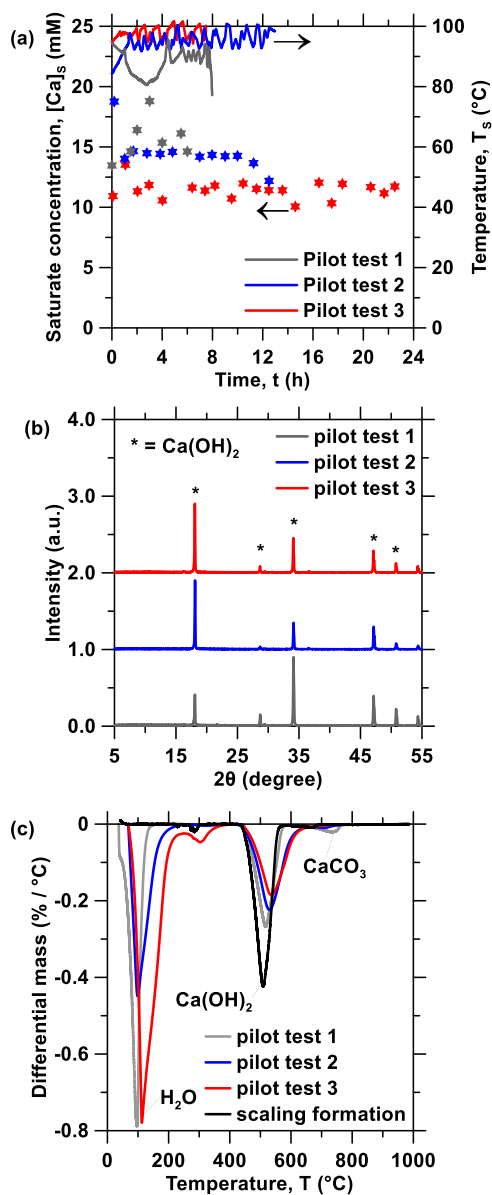


Fig. 9. (a) $[Ca]$ concentration and precipitation temperature T_s in the saturate stream as functions of time, (b) XRD, and (c) TGA-DTG spectrum of the solid precipitate from pilot tests 1, 2, and 3.

We hypothesized that supersaturation was possible without causing substantial membrane degradation because calcium concentration occurs instantaneously in the RO system at elevated flow rates whereas the kinetics of $Ca(OH)_2$ crystallization and precipitation from a saturated solution at room temperature is slow [56,57]. However, operating near portlandite saturation continuously increased scaling on the RO membranes by the formation of $Ca(OH)_2$ or $CaCO_3$ precipitates. Periodical flow reversal could improve the membrane's lifetime [58]. Additionally, anti-scaling coatings of polyethylene glycol (PEG) have been shown to reduce precipitate formation in BW30 Filmtec® membranes used in this study [59].

4.4. Precipitation and $Ca(OH)_2$ characterization

Following the concentration step, $Ca(OH)_2$ precipitated in a continuously stirred reactor maintained at a constant temperature of 95 ± 5 °C. Fig. 9 shows (a) the concentration of the recycled saturate stream $[Ca]_s$ – after filtering out the solid $Ca(OH)_2$ – as a function of time,

Table 2

Operating conditions and experimental results of $Ca(OH)_2$ precipitation in the three pilot tests performed.

	Pilot test 1	Pilot test 2	Pilot test 3
Average precipitation temperature T_s	88 °C	95 °C	98 °C
Test duration τ	8 h	12 h	24 h
Average residence time (V_{precip}/\dot{V}_s)	0.7 h	1.0 h	2.1 h
Collected mass of $Ca(OH)_2$ $m_{Ca(OH)_2,e}$	328.3 g	343.6 g	452.7 g
Production rate $\dot{m}_{Ca(OH)_2,e}$	41 g/h	28.6 g/h	18.8 g/h
Precipitation efficiency η_{PC}	62.6%	60.1%	79.2%
Purity of $Ca(OH)_2$	93.9%	95.9%	96.9%
Average saturate concentration $[Ca]_s$	15.6 mM	14.5 mM	11.4 mM
$Ca(OH)_2$ solubility at T_s ^a	14.6 mM	14.1 mM	13.9 mM

^a Calculated with PHREEQC using the minteq.v4 database [70].

(b) XRD pattern, and (c) TGA-DTG spectrum of the solid precipitates for all three pilot tests performed. Fig. 9(a) shows that the saturate concentration was strongly dependent on the precipitation temperature T_s . For example, at the beginning of pilot tests 1 and 2 when the precipitation temperature was below 90 °C, the calcium concentrations in solution $[Ca]_s$ increased, indicating a reduction in $Ca(OH)_2$ precipitation. On the other hand, the precipitation step was not affected by the retentate concentration $[Ca]_R$, which varied between around 20 mM \pm 5 mM [Fig. 8(c)].

Fig. 9(b) establishes that portlandite was the most abundant phase present in the solid precipitate recovered from the pilot tests. Note that, while XRD was performed on carefully crushed powders to reduce the potential for preferential orientation of the crystals, the XRD pattern were acquired in static conditions, i.e., using a non-rotating sample holder. Consequently, similar peak positions were observed but the peak intensities varied between pilot tests 1 and 2. These results were further confirmed by TGA-DTG, indicating that the $Ca(OH)_2$ content, calculated from its decomposition around 500 °C [35,60], made up 63–72 wt% of the analyzed precipitates. Water content represented 23–34 wt% of the solids [Fig. 9(c)]. An additional 2 wt% of the precipitates decomposed around 700 °C, corresponding to the presence of $CaCO_3$, undetected by XRD due to its small mass fraction. The latter may have formed because of the presence of dissolved CO_2 in the feed water [36] and/or, the brief contact of the wet $Ca(OH)_2$ precipitate with air during drying when it carbonated upon exposure to atmospheric CO_2 [61]. The remaining 2 wt % impurities appear to be composed of slag particulates. Compared with our previous benchtop experiments [17], the amount of $CaCO_3$ impurities was drastically reduced in the pilot system because the ratio of the volume of solution to the surface in contact with air was much larger. These results demonstrate that the purity of $Ca(OH)_2$ obtained with this pilot system paralleled that of commercial-grade hydrated lime [62].

Table 2 summarizes the conditions as well as the amount and purity of the $Ca(OH)_2$ precipitated for each test performed. A $Ca(OH)_2$ production rate of 41 g/h (equivalent to 1 kg per day) was obtained in pilot test 1, demonstrating the technical feasibility of the process at the pilot scale. Additionally, the precipitation efficiency – defined as the ratio of the theoretical and experimental production rates $\eta_{PC} = \dot{m}_{Ca(OH)_2}/\dot{m}_{Ca(OH)_2,e}$ – was the largest during pilot test 3. This coincided with a lower saturate calcium concentration $[Ca]_s$, indicating an improvement in the precipitation yield in pilot test 3. The purity of $Ca(OH)_2$ solids exceeded 93.9% in all cases. Table 2 indicates that the average saturate concentration $[Ca]_s$ measured experimentally was larger than the theoretical saturation concentration at precipitation temperature T_s in pilot tests 1 and 2, as expected. However, in pilot test 3, the saturate concentration $[Ca]_s$ was lower than the theoretical solubility limit. Indeed, variations in $Ca(OH)_2$ solubility across the literature consulted may be as much as \pm 5 mM [28,40]. In fact, $Ca(OH)_2$ solubility was found to be dependent on crystal size, the source material, and the solid dosage [29,63–65]. In the present study, differences between theoretical and experimental solubilities could be due to the presence of other

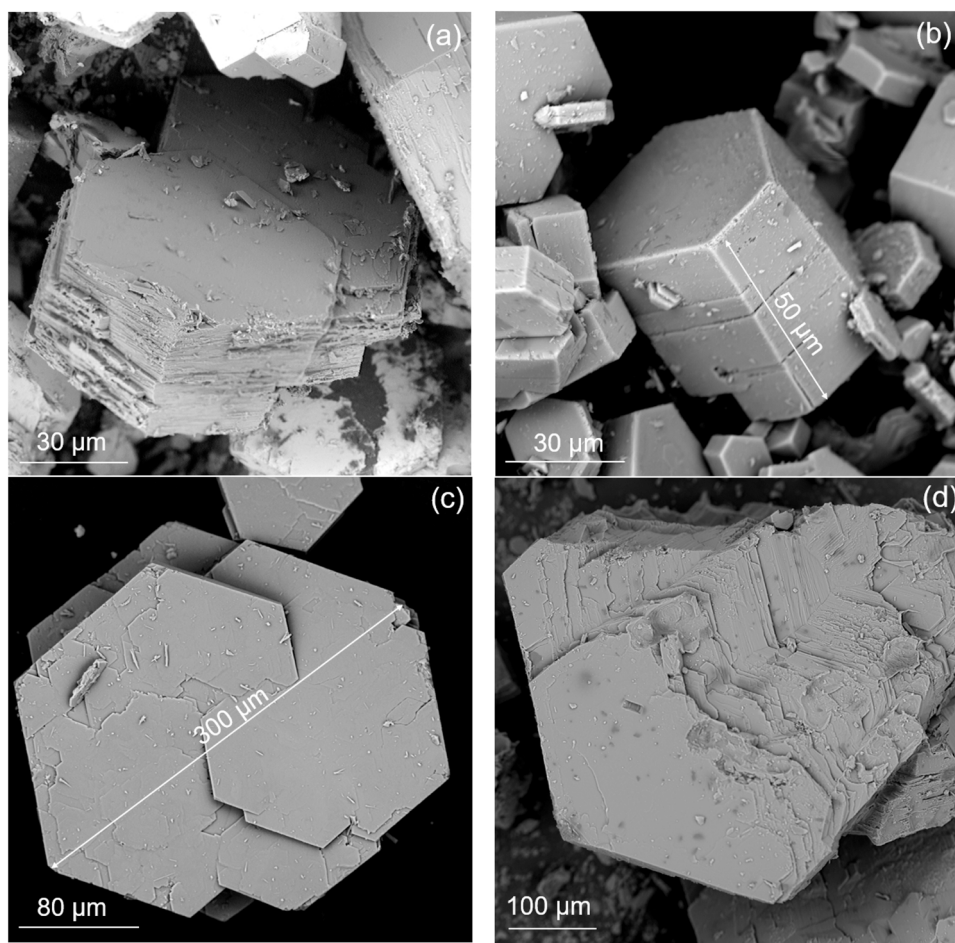


Fig. 10. SEM images of representative crystals filtered after precipitation in pilot (a) test 1, (b) test 2, (c) test 3, and (d) scaling formations on the surface of the heaters during pilot test 1.

cations in solution leached from slag and increasing the pH of the solution [25] – compared with pure $\text{Ca}(\text{OH})_2$ solutions – thus, shifting the equilibrium towards the formation of solid $\text{Ca}(\text{OH})_2$ [66]. Moreover, the different saturate concentrations $[\text{Ca}]_s$ at similar temperature (pilot tests 2 and 3) could be due to the different residence times in the reactor since kinetics plays an important role in precipitation reactions.

Fig. 10 shows SEM images of the crystals recovered from pilot (a) test 1, (b) test 2, (c) test 3 and (d) scaling formations on the surface of the heaters during pilot test 1. It is evident that all the precipitated crystals had hexagonal structures characteristic of $\text{Ca}(\text{OH})_2$ [61,67]. Fig. 10(c) indicates that the $\text{Ca}(\text{OH})_2$ crystals were larger in pilot test 3 than in the other tests. This observation was consistent with the larger residence time of ~ 2 h in the precipitation reactor compared with ~ 1 h in pilot tests 1 and 2 [57]. The smaller crystal size obtained during pilot tests 1 and 2 resulted in larger calcium concentration dissolved in solution $[\text{Ca}]_s$, since smaller crystals ($< 1 \mu\text{m}$) may have not been filtered out of the saturated solution and/or may have redissolved during the sampling procedure. In fact, coarser crystals display lower solubility than smaller crystals [63]. Thus, a longer residence time in the precipitation reactor results in larger crystal size and precipitation yield.

Moreover, a large fraction of the $\text{Ca}(\text{OH})_2$ crystals formed through heterogeneous precipitation at the surface of the heaters where the temperature was the largest. The scaling layer of $\text{Ca}(\text{OH})_2$ crystals on the heaters was approximately 1 mm thick and brittle which facilitated their recovery. As opposed to the $\text{Ca}(\text{OH})_2$ crystals collected in the filters, the crystals extracted from the surface of the heaters were larger (100–200 μm) and more disordered [Fig. 10(d)], and did not contain any water [Fig. 9(c)]. Nevertheless, they showed the same degree of

Table 3

Energy and specific energy consumption of the unit operations of the process for the pilot tests performed.

	Pilot test 1 (8 h)		Pilot test 2 (12 h)		Pilot test 3 (24 h)	
	Energy (kWh)	SEC (kWh / kg Ca (OH) ₂)	Energy (kWh)	SEC (kWh / kg Ca (OH) ₂)	Energy (kWh)	SEC (kWh / kg Ca (OH) ₂)
Grinding	0.787	2.397	0.828	2.410	0.975	2.154
Mixing	0.759	2.312	1.090	3.172	1.940	4.280
Heating	87.130	265.397	89.731	261.149	85.829	189.590
RO pump	0.631	1.920	0.690	2.008	0.362	0.798

purity as the crystals obtained from precipitation in solution [Fig. 9(c)]. Finally, $\text{Ca}(\text{OH})_2$ had also a strong tendency to form scaling on the walls of the precipitation reactor and of the downstream pipes. However, the mass of this precipitate was not quantified. Such scaling could be reduced by using scraped surface crystallizers and by minimizing the distance between the precipitation reactor and the solid/liquid separation system.

4.5. Energy consumption

A detailed energy balance analysis of the process was performed using Eqs. (2)–(7) and (14). Table 3 summarizes the mass and energy balance of each pilot tests. It indicates that the specific pumping power

consumption decreased when operating at lower pressures. The pumping electricity consumption calculated theoretically was 0.798 kWh/kg Ca(OH)₂. Table 3 shows that the grinding and mixing energies were as important as the energy required for pumping into the RO unit. The mixing energy consumption could be minimized with a careful design of the leaching and precipitation reactors and particularly by optimizing reactor volume, impeller diameter and rotation frequency. Additionally, since Ca(OH)₂ crystals growth has been shown to be independent of the stirring rate [64], the mixing energy could be reduced substantially. Although the grinding energy per kg of slag was low (0.016 kWh/kg slag), the low efficiency of calcium extraction during leaching (below 10%) caused a large grinding specific energy consumption (2.1 – 2.4 kWh/kg Ca(OH)₂), underscoring the importance of improving the calcium extraction from slag to decrease the energy consumption and CO₂ footprint of the process. Finally, the heating energy consumption was two orders of magnitude larger than the electricity consumption, as predicted by the model (Fig. 6). Nevertheless, at least 50% of this energy could be recovered using a heat exchanger to preheat the retentate solution entering the precipitation reactor based on process integration principles [68,69]. A future study should include a detailed discussion of the techno-economic feasibility of the scaled-up process and of the CO₂ footprint of the Ca(OH)₂ considering energy consumption, capital costs, and availability and cost of raw materials and waste heat.

5. Conclusion

This study demonstrated the design and continuous operation of a pilot system to produce Ca(OH)₂ from industrial alkaline wastes as feedstock. The process encompasses an integrated set of three unit operations including leaching, RO concentration, and temperature-swing precipitation. Water was fully recirculated, making the water consumption of the process virtually zero. Decreasing the slag particle size during leaching improved the calcium concentration of the leachate, thereby increasing calcium extraction from slag without the need to increase slag consumption. We also demonstrated the stability and reliability of the continuous process by completing three continuous tests of 8, 12, and 24 h using the same RO membranes. Fouling and/or scaling was reversed with standard membrane cleaning procedures. The low energy demand, and the reversibility of fouling demonstrated that RO is a robust technology to concentrate the slag leachates. Finally, larger residence times in the precipitation reactor increased the crystal particle size and decreased the calcium concentration of the saturated solution $[Ca]_s$, indicating an increase in the quantity of Ca(OH)₂ precipitated per unit volume of solution. An equivalent production rate of 1 kg per day was demonstrated during pilot test 1 whereas a continuous 24-hour operation was demonstrated during pilot test 3. In all cases, the purity of the Ca(OH)₂ exceeded 94%. Finally, process flow model and thermodynamic calculations agreed well with experimental measurements. Important control parameters have been identified to maximize Ca(OH)₂ production rate, to minimize energy consumption, and/or to control the size of Ca(OH)₂ particles.

CRedit authorship contribution statement

Sara Vallejo Castano: Conceptualization, Methodology, Formal analysis, Data curation, Visualization, Writing – original draft. **Marie Collin:** Resources, Investigation, Formal analysis, Validation. **Erika Callagon La Plante:** Methodology, Supervision, Conceptualization. Writing – review & editing. **Gaurav Sant:** Methodology, Supervision, Funding acquisition. **Laurent Pilon:** Conceptualization, Methodology, Formal analysis, Project administration, Supervision, Writing – review & editing, Supervision, Funding acquisition.

Declaration of Competing Interest

The authors declare that they have no known competing financial

interests or personal relationships that could have appeared to influence the work reported in this paper.

Acknowledgements

The authors acknowledge financial support for this research from the Department of Energy via: (a) The Office of Fossil Energy's National Energy Technology Laboratory (NETL: DE- FE0029825), (b) The Advanced Research Projects Agency-Energy (ARPA-E: DE-AR-0001147) and (c) TRANSCEND: a UCLA-NIST Consortium that is supported by its Industry and Agency partners (d) The National Science Foundation NRT-INFEWS: Integrated Urban Solutions for Food, Energy, and Water Management (Grant No. DGE-1735325). This research was conducted in the Morrin-Martinelli-Gier Memorial heat transfer laboratory, the Laboratory for Chemistry of Construction Materials (LC²) and the Molecular Instrumentation Center at UCLA. As such, the authors gratefully acknowledge all their researchers and the support that has made these laboratories and their operations possible. The authors would also like to acknowledge: Gabby Huffnagel (Stein, Inc.) for the supply of the BOF slag, the technical team from facilities management at UCLA for their assistance with the setting up the pilot system, and Boral Resources for their assistance with the XRF analysis of the slags. The contents of this paper reflect the views and opinions of the authors, who are responsible for the accuracy of the datasets presented herein, and do not reflect the views and/or policies of the agency, nor do the contents constitute a specification, standard or regulation.

Appendix A. Supporting information

Supplementary data associated with this article can be found in the online version at doi:10.1016/j.jece.2022.107792.

References

- [1] R.S. Boynton. *Chemistry and Technology of Lime and Limestone*, second ed., Wiley & Sons, New York, NY, 1980.
- [2] K. Vance, G. Falzone, I. Pignatelli, M. Bauchy, M. Balonis, G. Sant, Direct carbonation of Ca(OH)₂ using liquid and supercritical CO₂: implications for carbon-neutral cementation, *Ind. Eng. Chem. Res.* 54 (2015) 8908–8918, <https://doi.org/10.1021/acs.iecr.5b02356>.
- [3] Z. Wei, B. Wang, G. Falzone, E.C. La Plante, M.U. Okoronkwo, Z. She, T. Oey, M. Balonis, N. Neithalath, L. Pilon, G. Sant, Clinkering-free cementation by fly ash carbonation, *J. CO₂ Util.* 23 (2018) 117–127, <https://doi.org/10.1016/j.jcou.2017.11.005>.
- [4] A. Strand, E. Korotkova, S. Willför, J. Hakala, E. Lindstedt, The use of calcium hydroxide as alkali source in peroxide bleaching of kraft pulp, *Nord. Pulp Pap. Res. J.* 32 (2017) 444–451, <https://doi.org/10.3183/npprj-2017-32-03-p444-451>.
- [5] L. Semerjian, G.M. Ayoub, High-pH-magnesium coagulation–flocculation in wastewater treatment, *Adv. Environ. Res.* 7 (2003) 389–403, [https://doi.org/10.1016/S1093-0191\(02\)00009-6](https://doi.org/10.1016/S1093-0191(02)00009-6).
- [6] J. Leentvaar, M. Rebhun, Effect of magnesium and calcium precipitation on coagulation-flocculation with lime, *Water Res.* 16 (1982) 655–662, [https://doi.org/10.1016/0043-1354\(82\)90087-2](https://doi.org/10.1016/0043-1354(82)90087-2).
- [7] M. Stork, W. Meindersma, M. Overgaag, M. Neils, A competitive and efficient lime industry, EuLA – The European Lime Association, Brussels, Belgium, 2014. (http://www.euLa.eu/wp-content/uploads/2019/02/A-Competitive-and-Efficient-Lime-Industry-Technical-report-by-Ecofys_0.pdf).
- [8] J.A.H. Oates, *Lime and Limestone: Chemistry and Technology. Production and Uses*, Wiley-VCH, Weinheim, Germany, 1998.
- [9] M. Kenny, T. Oates, Lime and limestone, in: *Ullmann's Encyclopedia of Industrial Chemistry*, first ed., Wiley-VCH, Weinheim, Germany, 2000 https://doi.org/10.1002/14356007.a15_317.pub2.
- [10] S.-J. Han, M. Yoo, D.-W. Kim, J.-H. Wee, Carbon dioxide capture using calcium hydroxide aqueous solution as the absorbent, *Energy Fuels* 25 (2011) 3825–3834, <https://doi.org/10.1021/ef200415p>.
- [11] K.S. Lackner, C.H. Wendt, D.P. Butt, E.L. Joyce, D.H. Sharp, Carbon dioxide disposal in carbonate minerals, *Energy* 20 (1995) 1153–1170, [https://doi.org/10.1016/0360-5442\(95\)00071-N](https://doi.org/10.1016/0360-5442(95)00071-N).
- [12] I. Mehdipour, G. Falzone, E.C. La Plante, D. Simonetti, N. Neithalath, G. Sant, How microstructure and pore moisture affect strength gain in portlandite-enriched composites that mineralize CO₂, *ACS Sustain. Chem. Eng.* 7 (2019) 13053–13061, <https://doi.org/10.1021/acssuschemeng.9b02163>.
- [13] C. Shi, A.F. Jiménez, A. Palomo, New cements for the 21st century: the pursuit of an alternative to Portland cement, *Cem. Concr. Res.* 41 (2011) 750–763, <https://doi.org/10.1016/j.cemconres.2011.03.016>.

- [14] L.A. Corathers, Lime, U.S. Geological Survey (USGS), 2019. (<https://prd-wret.s3-us-west-2.amazonaws.com/assets/palladium/production/atoms/files/mcs-2019-lime.pdf>) (accessed October 26, 2019).
- [15] A. Dowling, J. O'Dwyer, C.C. Adley, Lime in the limelight, *J. Clean. Prod.* 92 (2015) 13–22, <https://doi.org/10.1016/j.jclepro.2014.12.047>.
- [16] C. Imboden, A. Komericki, A. Lyons, LafargeHolcim biodiversity, management plans and Karst Biodiversity Management, Fauna & Flora International, Cambridge, UK, 2018. (https://www.lafargeholcim.com/sites/lafargeholcim.com/files/atoms/files/2018_ffr_recommendations_asia_project_with_lafargeholcim.pdf) (accessed December 22, 2020).
- [17] S. Vallejo Castaño, E. Callagon La Plante, S. Shimoda, B. Wang, N. Neithalath, G. Sant, L. Pilon, Calcination-free production of calcium hydroxide at sub-boiling temperatures, *RSC Adv.* 11 (2021) 1762–1772, <https://doi.org/10.1039/D0RA08449B>.
- [18] G.N. Sant, L.G. Pilon, E.B.C.L. Callagon La Plante, B. Wang, Z. Wei, S. Vallejo Castaño, Facile, low-energy routes for the production of hydrated calcium and magnesium salts from alkaline industrial wastes, US20210024364A1, 2021. (<https://patents.google.com/patent/US20210024364A1/en>) (accessed March 29, 2021).
- [19] J.J. Chen, J.J. Thomas, H.F.W. Taylor, H.M. Jennings, Solubility and structure of calcium silicate hydrate, *Cem. Concr. Res.* 34 (2004) 1499–1519, <https://doi.org/10.1016/j.cemconres.2004.04.034>.
- [20] H.M. Jennings, Aqueous solubility relationships for two types of calcium silicate hydrate, *J. Am. Ceram. Soc.* 69 (1986) 614–618, <https://doi.org/10.1111/j.1151-2916.1986.tb04818.x>.
- [21] C.S. Walker, S. Sutou, C. Oda, M. Mihara, A. Honda, Calcium silicate hydrate (C-S-H) gel solubility data and a discrete solid phase model at 25 °C based on two binary non-ideal solid solutions, *Cem. Concr. Res.* 79 (2016) 1–30, <https://doi.org/10.1016/j.cemconres.2015.07.006>.
- [22] R.S. Iyer, J.A. Scott, Power station fly ash — a review of value-added utilization outside of the construction industry, *Resour. Conserv. Recycl.* 31 (2001) 217–228, [https://doi.org/10.1016/S0921-3449\(00\)00084-7](https://doi.org/10.1016/S0921-3449(00)00084-7).
- [23] F. Zhang, H. Itoh, Extraction of metals from municipal solid waste incinerator fly ash by hydrothermal process, *J. Hazard. Mater.* 136 (2006) 663–670, <https://doi.org/10.1016/j.jhazmat.2005.12.052>.
- [24] M. Loncar, H.A. van der Sloot, A. Mladenović, M. Zupancić, L. Kobal, P. Bukovec, Study of the leaching behaviour of ladle slags by means of leaching tests combined with geochemical modelling and mineralogical investigations, *J. Hazard. Mater.* 317 (2016) 147–157, <https://doi.org/10.1016/j.jhazmat.2016.05.046>.
- [25] L. De Windt, P. Chaurand, J. Rose, Kinetics of steel slag leaching: batch tests and modeling, *Waste Manag.* 31 (2011) 225–235, <https://doi.org/10.1016/j.wasman.2010.05.018>.
- [26] N.M. Piatak, M.B. Parsons, R.R. Seal, Characteristics and environmental aspects of slag: a review, *Appl. Geochem.* 57 (2015) 236–266, <https://doi.org/10.1016/j.apgeochem.2014.04.009>.
- [27] L. Malaeb, G.M. Ayoub, Reverse osmosis technology for water treatment: state of the art review, *Desalination* 267 (2011) 1–8, <https://doi.org/10.1016/j.desal.2010.09.001>.
- [28] PHREEQC, Version 3, U.S. Geological Survey, 2017. (<https://www.usgs.gov/software/versions/phreeqc-version-3>).
- [29] R.G. Bates, V.E. Bower, E.R. Smith, Calcium hydroxide as a highly alkaline pH standard, *J. Res. Natl. Bur. Stand.* 56 (1956) 305–312, <https://doi.org/10.6028/jres.056.040>.
- [30] Y. Ghasemi, M. Emborg, A. Cwirzen, Estimation of specific surface area of particles based on size distribution curve, *Mag. Concr. Res.* 70 (2018) 533–540, <https://doi.org/10.1680/jmacr.17.00045>.
- [31] C. Thomas, J. Rosales, J.A. Polanco, F. Agrela, Steel slags, in: *New Trends in Eco-Efficient and Recycled Concrete*, Elsevier, Cambridge, U.S.A., 2019, pp. 169–190, <https://doi.org/10.1016/B978-0-08-102480-5.00007-5>.
- [32] Y.-L. Chen, C.-T. Lin, Recycling of basic oxygen furnace slag as a raw material for autoclaved aerated concrete production, *Sustainability* 12 (2020) 5896, <https://doi.org/10.3390/su12155896>.
- [33] I.Z. Yildirim, M. Prezzi, Chemical, mineralogical, and morphological properties of steel slag, *Adv. Civ. Eng.* 2011 (2011) 1–13, <https://doi.org/10.1155/2011/463638>.
- [34] R. Gabrovšek, T. Vuk, V. Kaučič, Evaluation of the hydration of portland cement containing various carbonates by means of thermal analysis, *Acta Chim. Slov.* 53 (2006) 159–165.
- [35] M. Khachani, A.E. Hamidi, M. Halim, S. Arsalane, Non-isothermal kinetic and thermodynamic studies of the dehydroxylation process of synthetic calcium hydroxide Ca(OH)₂, *J. Mater. Environ. Sci.* 5 (2014) 615–624.
- [36] M.-A. Popescu, R. Isopescu, C. Matei, G. Fagarasan, V. Plesu, Thermal decomposition of calcium carbonate polymorphs precipitated in the presence of ammonia and alkylamines, *Adv. Powder Technol.* 25 (2014) 500–507, <https://doi.org/10.1016/j.apt.2013.08.003>.
- [37] F.C. Bond, Crushing and grinding calculations, *Br. Chem. Eng.* 6 (1961) 378–385.
- [38] N.L. Weiss, Society of Mining Engineers of AIME, SME Mineral Processing Handbook, Society of Mining Engineers of the American Institute of Mining, Metallurgical, and Petroleum Engineers, New York, NY, 1985.
- [39] P.M. Doran, *Bioprocess Engineering Principles*, second ed., Elsevier, Oxford, UK, 2013.
- [40] AspenONE (Version 10), Aspen Technology, Inc., 2017. (<https://www.aspentech.com/en/products/engineering/aspens-plus>).
- [41] S.-Y. Pan, P.-C. Chiang, Y.-H. Chen, C.-D. Chen, H.-Y. Lin, E.-E. Chang, Systematic approach to determination of maximum achievable capture capacity via leaching and carbonation processes for alkaline steelmaking wastes in a rotating packed bed, *Environ. Sci. Technol.* 47 (2013) 13677–13685, <https://doi.org/10.1021/es403323x>.
- [42] R.W. Fox, A.T. McDonald, P.J. Pritchard, *Introduction to Fluid Mechanics*, eighth ed., John Wiley & Sons Inc., Hoboken, NJ, 2011.
- [43] M. Mulder, *Basic Principles of Membrane Technology*, first ed., Springer, Dordrecht, Netherlands, 1991 <https://doi.org/10.1007/978-94-017-0835-7>.
- [44] E. Dražević, K. Košutić, V. Freger, Permeability and selectivity of reverse osmosis membranes: correlation to swelling revisited, *Water Res.* 49 (2014) 444–452.
- [45] H. Dach, Comparison of nanofiltration and reverse osmosis processes for a selective desalination of brackish water feeds, Université d'Angers, 2008. (<https://tel.archives-ouvertes.fr/tel-00433513>).
- [46] W. Lawler, T. Wijaya, A. Antony, G. Leslie, P. Le-Clech, Reuse of reverse osmosis desalination membranes, in: *IDA World Congress*, Perth, Western Australia, 2011.
- [47] Y.S. Oren, P.M. Biesheuvel, Theory of ion and water transport in reverse-osmosis membranes, *Phys. Rev. Appl.* 9 (2018), 024034, <https://doi.org/10.1103/PhysRevApplied.9.024034>.
- [48] T.L. Bergman, A.S. Lavine, F.P. Incropera, D.P. Dewitt, *Fundamentals of Heat and Mass Transfer*, seventh ed., Wiley & Sons, Hoboken, NJ, 2011.
- [49] D.B. Gingerich, M.S. Mauter, Quantity, quality, and availability of waste heat from United States thermal power generation, *Environ. Sci. Technol.* 49 (2015) 8297–8306, <https://doi.org/10.1021/es5060989>.
- [50] C. Shi, J. Qian, High performance cementing materials from industrial slags — a review, *Resour., Conserv. Recycl.* 29 (2000) 195–207, [https://doi.org/10.1016/S0921-3449\(99\)00060-9](https://doi.org/10.1016/S0921-3449(99)00060-9).
- [51] E. Belhadj, C. Diliberto, A. Lecomte, Characterization and activation of basic oxygen furnace slag, *Cem. Concr. Compos.* 34 (2012) 34–40, <https://doi.org/10.1016/j.cemconcomp.2011.08.012>.
- [52] J.-M. Gautier, E.H. Oelkers, J. Schott, Are quartz dissolution rates proportional to B.E.T. surface areas? *Geochim. Et. Cosmochim. Acta* 65 (2001) 1059–1070, [https://doi.org/10.1016/S0016-7037\(00\)00570-6](https://doi.org/10.1016/S0016-7037(00)00570-6).
- [53] W.L. Ebert, The effects of the glass surface area/solution volume ratio on glass corrosion: A critical review, Argonne National, Lab. Argonne IL (1995), <https://doi.org/10.2172/67461>.
- [54] E.M.V. Hoek, A.S. Kim, M. Elimelech, Influence of crossflow membrane filter geometry and shear rate on colloidal fouling in reverse osmosis and nanofiltration separations, *Environ. Eng. Sci.* 19 (2002) 357–372, <https://doi.org/10.1089/109287502320963364>.
- [55] X. Zhu, M. Elimelech, Colloidal fouling of reverse osmosis membranes: measurements and fouling mechanisms, *Environ. Sci. Technol.* 31 (1997) 3654–3662, <https://doi.org/10.1021/es970400v>.
- [56] D. Klein, Homogeneous nucleation of calcium hydroxide, *Talanta* 15 (1968) 229–231, [https://doi.org/10.1016/0039-9140\(68\)80227-9](https://doi.org/10.1016/0039-9140(68)80227-9).
- [57] H. Furedi-Milhofer, Spontaneous precipitation from electrolytic solutions, *Pure Appl. Chem.* 53 (1981) 2041–2055, <https://doi.org/10.1351/pac198153112041>.
- [58] M. Uchymiak, A.R. Bartman, N. Daltrophe, M. Weissman, J. Gilron, P. D. Christofides, W.J. Kaiser, Y. Cohen, Brackish water reverse osmosis (BWRO) operation in feed flow reversal mode using an ex situ scale observation detector (EXSOD), *J. Membr. Sci.* 341 (2009) 60–66, <https://doi.org/10.1016/j.memsci.2009.05.039>.
- [59] J.R. Ray, W. Wong, Y.-S. Jun, Antiscalcing efficacy of CaCO₃ and CaSO₄ on polyethylene glycol (PEG)-modified reverse osmosis membranes in the presence of humic acid: interplay of membrane surface properties and water chemistry, *Phys. Chem. Chem. Phys.* 19 (2017) 5647–5657, <https://doi.org/10.1039/C6CP08569E>.
- [60] R. Gabrovšek, T. Vuk, V. Kaučič, Evaluation of the hydration of Portland cement containing various carbonates by means of thermal analysis, *Acta Chim. Slov.* 53 (2006) 159–165.
- [61] E. Ruiz-Agudo, K. Kudlacz, C.V. Putnis, A. Putnis, C. Rodriguez-Navarro, Dissolution and carbonation of portlandite [Ca(OH)₂] single crystals, *Environ. Sci. Technol.* 47 (2013) 11342–11349, <https://doi.org/10.1021/es402061c>.
- [62] D. Lesueur, J. Petit, H.-J. Ritter, The mechanisms of hydrated lime modification of asphalt mixtures: a state-of-the-art review, *Road. Mater. Pavement Des.* 14 (2013) 1–16, <https://doi.org/10.1080/14680629.2012.743669>.
- [63] L.B. Miller, J.C. Witt, Solubility of calcium hydroxide, *J. Phys. Chem.* 33 (1929) 285–289, <https://doi.org/10.1021/j150296a010>.
- [64] M.E. Tadros, J. Skalny, R.S. Kalyoncu, Kinetics of calcium hydroxide crystal growth from solution, *J. Colloid Interface Sci.* 55 (1976) 20–24, [https://doi.org/10.1016/0021-9797\(76\)90004-7](https://doi.org/10.1016/0021-9797(76)90004-7).
- [65] K. Johannsen, S. Rademacher, Modelling the kinetics of calcium hydroxide dissolution in water, *Acta Hydrochim. Et. Hydrobiol.* 27 (1999) 72–78, [https://doi.org/10.1002/\(SICI\)1521-401X\(199902\)27:2<72::AID-AHEH72>3.0.CO;2-H](https://doi.org/10.1002/(SICI)1521-401X(199902)27:2<72::AID-AHEH72>3.0.CO;2-H).
- [66] J. Duchesne, E.J. Reardon, Measurement and prediction of portlandite solubility in alkali solutions, *Cem. Concr. Res.* 25 (1995) 1043–1053, [https://doi.org/10.1016/0008-8846\(95\)00099-X](https://doi.org/10.1016/0008-8846(95)00099-X).
- [67] C. Rodriguez-Navarro, E. Hansen, W.S. Ginell, Calcium hydroxide crystal evolution upon aging of lime putty, *J. Am. Ceram. Soc.* 81 (2005) 3032–3034, <https://doi.org/10.1111/j.1151-2916.1998.tb02735.x>.
- [68] I.C. Kemp, Reducing dryer energy use by process integration and pinch analysis, *Dry. Technol.* 23 (2005) 2089–2104, <https://doi.org/10.1080/07373930500210572>.
- [69] J.C. Atuonwu, G. van Straten, H.C. van Deventer, A.J.B. van, Optimizing, Energy efficiency in low temperature drying by zeolite adsorption and process integration, *Chem. Eng. Trans.* 25 (2011) 111–116, <https://doi.org/10.3303/CET1125019>.
- [70] David L Parkhurst, C.A.J Appelo, chap. A43, Description of input and examples for PHREEQC version 3—A computer program for speciation, batch-reaction, one-dimensional transport, and inverse geochemical calculations: U.S. Geological Survey Techniques and Methods, USGS, 2013.